Preprint No. 2019-02

Parameterization of arbitrary hole shapes using non-destructive testing and resulting stress concentration in a 2D plate with finite dimensions

M. Drieschner*[1], Y. Petryna[1], L. Eichner[1]

February 22, 2019

*Correspondence: M. Drieschner: martin.drieschner@tu-berlin.de
[1]Technische Universität Berlin, Faculty VI Planning Building Environment, Department of Civil Engineering, Chair of Structural Mechanics, Gustav-Meyer-Allee 25, 13355 Berlin, Germany

Suggested Citation: M. Drieschner, Y. Petryna, L. Eichner. Parameterization of arbitrary hole shapes using non-destructive testing and resulting stress concentration in a 2D plate with finite dimensions. *Preprint-Reihe des Fachgebiets Statik und Dynamik, Technische Universität Berlin*, Preprint No. 2019-02, 2019. http://dx.doi.org/10.14279/depositonce-8236.

Preprint-Reihe des Fachgebiets Statik und Dynamik, Technische Universität Berlin auf https:// depositonce.tu-berlin.de/

Parameterization of arbitrary hole shapes using non-destructive testing and resulting stress concentration in a 2D plate with finite dimensions

M. Drieschner, Y. Petryna, L. Eichner

Abstract

Air void inclusions are mostly unavoidable in many different materials resulting from manufacturing processes or environmental conditions. In this contribution, non-destructive testing (NDT) like computer tomography (CT) is used for air void detection and quantification. The air voids lead to stress concentrations around them which influence significantly the structural integrity and at worst, lead to structural failure. By nature, air voids exhibit arbitrary shapes on which circular, elliptical, slotted and rounded rectangular holes are fitted by a least-square optimization algorithm to reduce the amount of necessary shape parameters. The mentioned shapes are compared in relation to the arbitrary one and with regard to the resulting stress concentration factor as well as the location of the maximum first principal stress in a 2D plate with finite dimensions under uniaxial tension. Finally, aleatory and epistemic uncertainties are derived from the conducted CT analysis which leads to a problem under polymorphic uncertainties. The problem is solved by a surrogate model based on cubic spline interpolation and points out the importance of the consideration of different hole shapes for analyzing the stress concentration.

Keywords *stress concentration factor; shape fitting; shape parameterization; polymorphic uncertainties*

1 Introduction

This study has been performed within the research project MuScaBlaDes – "Multi-scale failure analysis with polymorphic uncertainties for optimal design of rotor blades" – which is part of the Priority Programme (SPP 1886) "Polymorphic uncertainty modelling for the numerical design of structures" started in 2016.

A linear elastic solution for stresses around a circular hole in a 2D plate with infinite dimensions was first of all presented by Ernst Gustav Kirsch in 1898 [13]. In the last century, further analytical solutions have been developed, e.g. for multiple holes, plates with finite dimensions, holes or notches of different shapes. In [20], an extensive overview with a broad spectrum of investigations is given of which some examples are used for comparison and are extended in this contribution. In all cases, stress concentrations around the holes or on the notches are present. In engineering applications, they can influence significantly the structural integrity and at worst, lead to structural failure.

The focus of the research project MuScaBlaDes is on air void inclusions in adhesive bonds of rotor blades caused by inaccuracies and imperfections in manufacturing processes. The reduced adhesive bond quality can lead to debonding, which has been identified as a significant reason for structural collapse in a full-scale rotor blade test [28] according to [11]. In this regard, sub-components, e.g. the Henkel beam by the Fraunhofer Institute for Wind Energy and Energy System Technology (IWES), have been developed in the past for detailed experimental investigations [21, 29]. For understanding the reasons of failure initiated by multiple cracks in the adhesive bonds, various NDT like ultrasonic (US) or computer tomographic (CT) scanning

have been applied by *Technische Universität Berlin* within the collaborative research project "BladeTester - Automated approach for serial integrity tests of rotor blades of wind turbines" (2011-2015) [19]. Various air voids of arbitrary shapes and different sizes are detectable, see section 2, whereby uncertainties in the data acquisition and data processing lead also to uncertain air void properties.

For investigations on the stress concentration factor and the location of the maximum first principal stress, a 2D linear elastostatic boundary value problem for a perforated structure is defined in section 3. Various hole shapes are presented and analyzed by means of a finite element approach. Available reference values, e.g. in [13, 20, 24, 10, 22, 12, 23], are used for validation and verification of the used finite element model.

In section 4, two holes of arbitrary shape detected in the conducted CT analysis are analyzed with regard to the resulting stress concentration. A least-square optimization algorithm is used to fit shapes with much less parameters on these. On the one hand, the shape fitting and on the other hand, the approximation of the stress concentration are compared.

Caused by the mentioned uncertain data acquisition with resulting uncertain hole shapes and their associated parameters, the extension to a problem under polymorphic uncertainties is finally presented in section 5. Randomness and natural variability as well as limited information, subjectivity and imprecise data lead to aleatory (*alea* (latin) = gambling, dice) and epistemic ($\epsilon\pi\iota\sigma\tau\acute{\eta}\mu\eta$ (greek) = science, profession) uncertainties, respectively [9, 18]. As an extension to probabilistic approaches [16, 27, 1, 14], the diversity of the uncertainty sources is considered, see [2] for an overview about possible models. In this study, stochastic and fuzzy variables are used at once like in [25, 26]. Results from a classical sampling approach are compared to those from a surrogate model before conclusions in section 6 and an outlook in section 7 are given.

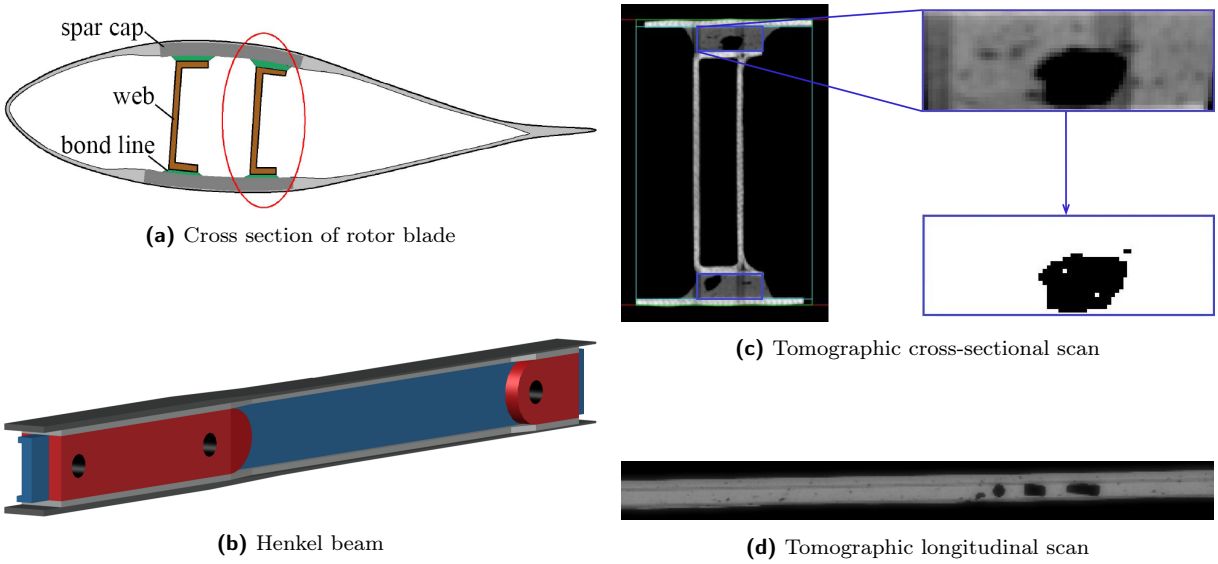

(a) Cross section of rotor blade

(b) Henkel beam

(c) Tomographic cross-sectional scan

(d) Tomographic longitudinal scan

Figure 1: Henkel beam relation to rotor blade according to [21] and CT scans

2 Computer tomographic scans of air voids in adhesive bonds

Rotor blades of wind turbines are thin-walled spatial structures typically consisting of two composite shells and one or two shear webs assembled with adhesive bonds, see Fig. 1a. As the overall integrity is affected by the quality of adhesive bonds, the focus in this contribution is on the failure of the latter. Due to the manufacturing process, air voids with a-priori uncertain properties are always present and can significantly reduce the strength of adhesive bonds. Regarding this, mechanical tests at coupon level with bond thicknesses of both $t = 0.5$mm and

$t = 3.0$mm are required in international standards as [11] for material certification even though not realistic for practical rotor blade design with bond thicknesses up to $t = 10$mm [21, 29]. To close the gap between full-scale and coupon tests, the Henkel beam has been developed as a representative sub-component for detailed investigations on adhesive bonds, see Fig. 1b.

In cooperation with the Fraunhofer IWES, ten Henkel beams have been used for various studies of adhesive bonds within the BladeTester project [19]. Non-destructive techniques (NDT) have been applied before and after fatigue tests on several Henkel beams [15]. Three of them - namely HB3, HB9 and HB10 - have been scanned by computer tomography (CT) to detect and analyze the air void properties *shape*, *size*, *location* and *orientation*. A cross-sectional scan in Fig. 1c and a longitudinal scan in Fig. 1d are exemplarily displayed. The data acquisition including the image processing depends on the chosen methods and present conditions, see [6] for more details and Fig. 2 for an application-related flowchart. The focus in the following is on the mathematical description of perforated structures using arbitrary as well as simplified shapes and on the resulting stress concentration around the hole which is critical for structural failure.

Figure 2: Application-related strategy for data handling and integration in numerical uncertainty models

3 Mathematical description of perforated structures

3.1 Numerical model

Based on section 2, a spatial model with a length of L in x-direction and a cross-section with a width of W in y-direction and a thickness of T in z-direction is defined, see Fig. 3.

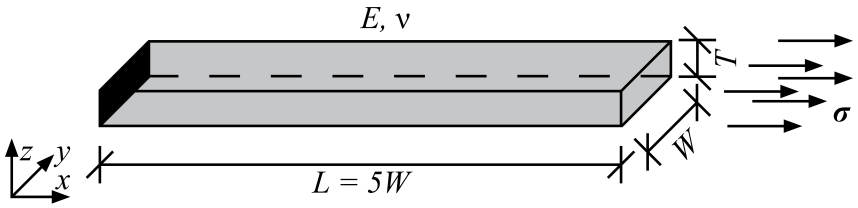

Figure 3: Unperforated 3D structure D

The thickness T is significant smaller than L and W, so the resulting three-dimensional cuboid is simplified to a rectangular two-dimensional plate with constant thickness T to avoid time-consuming numerical simulations. In this unperforated domain D with boundary ∂D, a single hole H with boundary ∂H is considered which has to comply with the following constraints.

(**A1**) H has an intersection with D of positive measure.

(**A2**) H has to keep a distance of $\delta \geq W$ away from the boundary ∂D in x-direction.

(**A3**) H has to keep a distance of $\delta > 0$ away from the boundary ∂D in y-direction.

Then based on (**A1**)-(**A3**),

$$\begin{aligned} D_{\mathrm{H}} &:= B \setminus H \\ \text{with} \quad B &= D\left(W \leq x \leq L - W\right) \\ \text{and boundary} \quad \partial D_{\mathrm{H}} &:= \partial D \cup \partial H \end{aligned} \tag{1}$$

is our perforated domain.

The two-dimensional plate under plane stress is fixed on the left at $x = 0$ and uniformly loaded in x-direction on the right at $x = L$, see Fig. 4a. Defining isotropic material with Young's modulus E and Poisson's ratio ν as well as linear elastic behavior leads to the linear elastostatic boundary value problem without body forces

$$\begin{aligned} \mathbf{0} &= \operatorname{div} \boldsymbol{\sigma} && \text{equilibrium equation in } D_{\mathrm{H}} \\ \boldsymbol{\epsilon} &= \left[\nabla \boldsymbol{u} + \nabla^{\mathrm{T}} \boldsymbol{u}\right]/2 && \text{strain-displacement equation in } D_{\mathrm{H}} \\ \boldsymbol{\sigma} &= \boldsymbol{C} : \boldsymbol{\epsilon} && \text{constitutive equation in } D_{\mathrm{H}} \\ \boldsymbol{u} &= \mathbf{0} && \text{Dirichlet boundary condition on } \partial D_{\mathrm{H}}\,(x = 0) \\ \boldsymbol{\sigma} \cdot \boldsymbol{n} &= \mathbf{0} && \text{Neumann boundary condition on } \partial D_{\mathrm{H}}\,(x < L) \\ \boldsymbol{\sigma} \cdot \boldsymbol{n} &= (1,0)^{\mathrm{T}} && \text{Neumann boundary condition on } \partial D_{\mathrm{H}}\,(x = L) \end{aligned} \tag{2}$$

which is solved within a finite element simulation.

The domain D_{H} is meshed by two-dimensional 8-node elements with quadratic displacement behavior. Depending on the hole properties, the structure is divided into critical and uncritical sections, see Fig. 4b. Uncritical sections are meshed with an element length of 10% of the plate width W. 0.1% of W is the respective element length for critical sections, meaning areas around the hole and at critical parts of the boundary. Some of these critical areas have been refined to secure a proper solution convergence.

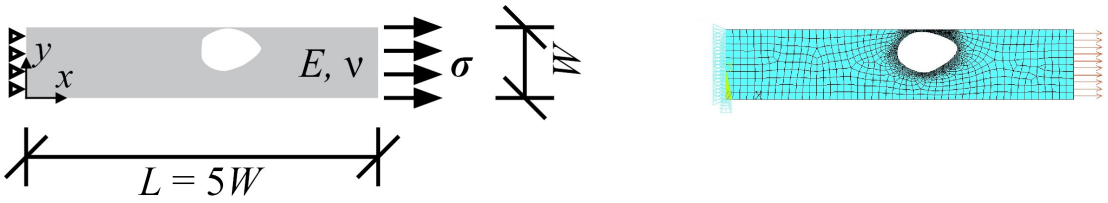

(a) Perforated 2D structure D_H **(b)** Numerical model

Figure 4: Perforated 2D structure and corresponding numerical model

From the resulting displacement vector $\boldsymbol{u}$, the maximum first principal stress σ_max and its location $\boldsymbol{x}_\mathrm{max}$ are calculated as follows:

$$\begin{aligned} \sigma_\mathrm{max} &= \operatorname*{ess\,sup}_{\boldsymbol{x}\in D_\mathrm{H}} \lambda_\mathrm{max}(\boldsymbol{\sigma}(\boldsymbol{u})[\boldsymbol{x}]), \\ \boldsymbol{x}_\mathrm{max} &= \operatorname*{arg\,max}_{\boldsymbol{x}\in D_\mathrm{H}} \sigma_\mathrm{max}. \end{aligned} \tag{3}$$

Here λ_max denotes the largest eigenvalue of $\boldsymbol{\sigma}$. As quantity of interest, a stress concentration factor

$$K_\mathrm{tg} = \frac{\sigma_\mathrm{max}}{\sigma} \tag{4}$$

is defined to quantify the influence of the hole on the structural stress [20]. Furthermore, the location $\boldsymbol{x}_\mathrm{max}$ is classified to:

$$c\left(\boldsymbol{x}_\mathrm{max}\right) = \begin{cases} \text{above}, & \text{if } \boldsymbol{x}_\mathrm{max} \text{ is located above the hole } H \\ \text{below}, & \text{if } \boldsymbol{x}_\mathrm{max} \text{ is located below the hole } H \end{cases} \tag{5}$$

3.2 Parameterizations of a two-dimensional hole

The described outcomes $K_\mathrm{tg} = \sigma_\mathrm{max}/\sigma$ and $c\left(\boldsymbol{x}_\mathrm{max}\right)$ depend on the hole shape s and its parameters $\boldsymbol{p}$ for location, size and orientation. In this study, several shape types are defined, see Fig. 5, for which the respective parameters are explained in an extensive manner below. For all cases, the finite plate length L and the location in x-direction have no influence on K_tg due to the unperforated edge regions [24], see Eq. (1).

3.2.1 Arbitrary hole and convex hull

The most general case for a hole shape is an entirely arbitrary one, which is defined by an infinite number of points $\boldsymbol{p} = (x_i, y_i)$, see Fig. 5a. The convex hull as smallest possible convex area including all points can be determined for concave shapes as shown in Fig. 5b. This can be parameterized alternatively by the hole centroid $(x_\mathrm{M}, y_\mathrm{M})$ and multiple axes with radius r_i and angle θ_i connecting the hole centroid with points on the hole boundary. For simple cases, a finite number of points is also sufficient, e.g. connected piecewise linearly or by splines [7].

3.2.2 Circular hole

Only three parameters $\boldsymbol{p} = (x_\mathrm{M}, y_\mathrm{M}, d)$ are needed to define a circular hole in a two-dimensional plate: the centroid coordinates $(x_\mathrm{M}, y_\mathrm{M})$ for the location and the radius r, or respectively, the diameter d for the size, see Fig. 5c. For validation of the presented numerical model, the stress concentration factor $K_\mathrm{tg} = K_\mathrm{tg}\left(x_\mathrm{M}, y_\mathrm{M}, d\right)$ is analyzed first for a centric hole with $y_\mathrm{M} = W/2$ and varying diameter $d \in (0, W)$, and second, for an eccentric hole with $d = W/4$ and varying y-coordinate of the centroid $y_\mathrm{M} \in (W/8, W/2]$, see Fig. 6. For the first case in Fig. 6a, the reference solution in green is given by [10]:

$$K_\mathrm{tg} = 0.284 + \frac{2}{1 - d/W} - 0.6\left(1 - \frac{d}{W}\right) + 1.32\left(1 - \frac{d}{W}\right)^2 \tag{6}$$

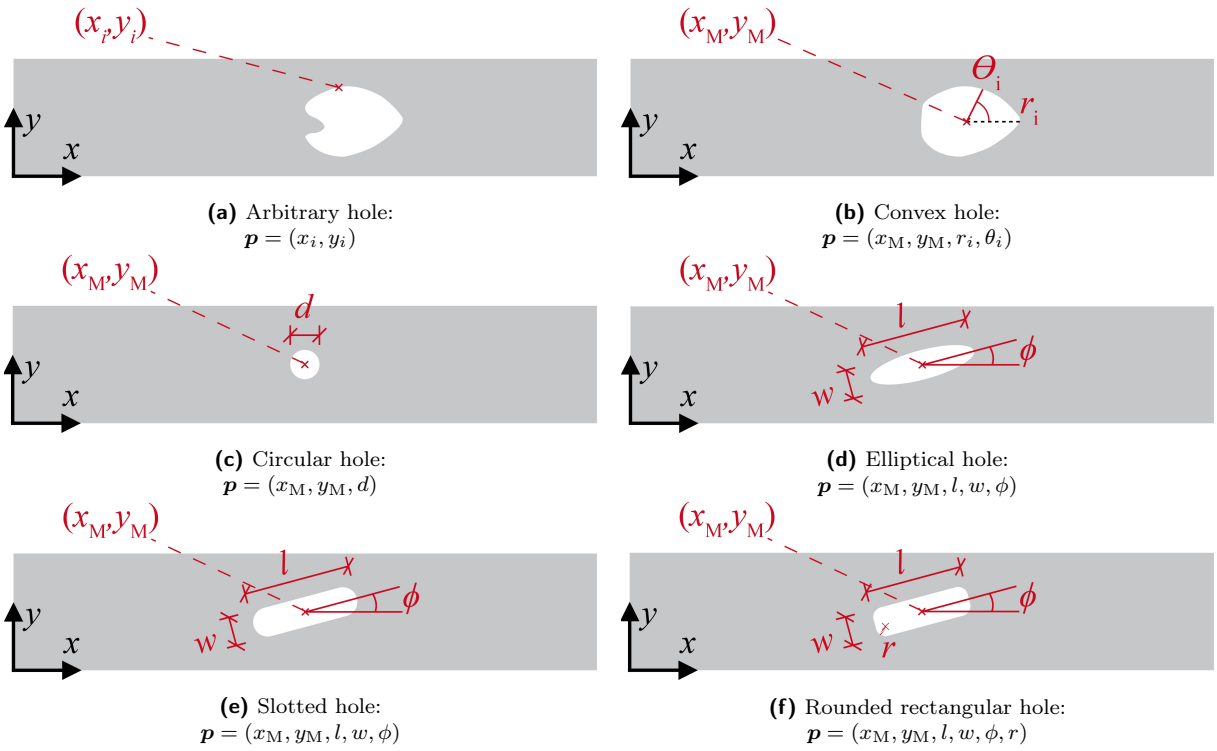

(a) Arbitrary hole: $\boldsymbol{p} = (x_i, y_i)$

(b) Convex hole: $\boldsymbol{p} = (x_\mathrm{M}, y_\mathrm{M}, r_i, \theta_i)$

(c) Circular hole: $\boldsymbol{p} = (x_\mathrm{M}, y_\mathrm{M}, d)$

(d) Elliptical hole: $\boldsymbol{p} = (x_\mathrm{M}, y_\mathrm{M}, l, w, \phi)$

(e) Slotted hole: $\boldsymbol{p} = (x_\mathrm{M}, y_\mathrm{M}, l, w, \phi)$

(f) Rounded rectangular hole: $\boldsymbol{p} = (x_\mathrm{M}, y_\mathrm{M}, l, w, \phi, r)$

Figure 5: Considered hole shapes s with parameters $\boldsymbol{p}$

For the second case in Fig. 6b, the reference solution in green is given by [22]:

$$K_\mathrm{tg} = \left(C_1 + C_2 \left(\frac{d}{2y_\mathrm{M}} \right) + C_3 \left(\frac{d}{2y_\mathrm{M}} \right)^2 \right) f_\mathrm{nom} \tag{7}$$

with

$$\begin{aligned} C_1 &= 2.989 - 0.0064 \tfrac{y_\mathrm{M}}{W - y_\mathrm{M}} \\ C_2 &= -2.872 + 0.095 \tfrac{y_\mathrm{M}}{W - y_\mathrm{M}} \\ C_3 &= 2.348 + 0.196 \tfrac{y_\mathrm{M}}{W - y_\mathrm{M}} \\ f_\mathrm{nom} &= \frac{\sqrt{1-(d/(2y_\mathrm{M}))^2}}{1-d/(2y_\mathrm{M})} \frac{1-y_\mathrm{M}/W}{1-y_\mathrm{M}/W \left[2-\sqrt{1-(d/(2y_\mathrm{M}))^2}\right]} \end{aligned}$$

As can be seen, the finite plate width is negligible for small and centric holes, so K_tg converges to 3 as solution for a circular hole in a plate with infinite width [13], otherwise the stress concentration increases rapidly to infinity.

3.2.3 Elliptical hole

An elliptical hole is parameterized by the centroid coordinates $(x_\mathrm{M}, y_\mathrm{M})$, the size parameters (l, w) and the rotation angle ϕ in the x-y-plane, see Fig. 5d. In Fig. 7, the evaluation of the stress concentration factor $K_\mathrm{tg} = K_\mathrm{tg}\,(x_\mathrm{M}, y_\mathrm{M}, l, w, \phi)$ is shown in which the reference solutions are given by [12]:

$$K_\mathrm{tg} = \left(C_1 + C_2 \left(\frac{w}{2y_\mathrm{M}} \right) + C_3 \left(\frac{w}{2y_\mathrm{M}} \right)^2 + C_4 \left(\frac{w}{2y_\mathrm{M}} \right)^3 \right) f_\mathrm{nom} \tag{8}$$

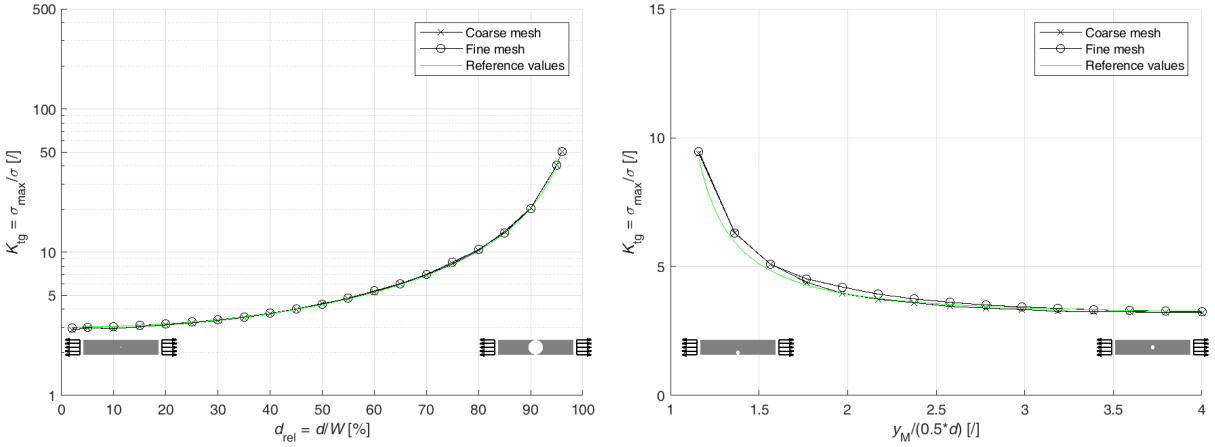

(a) $\boldsymbol{p} = (x_\mathrm{M}, y_\mathrm{M}, d) = \left(\frac{L}{2}, \frac{W}{2}, d\right)$ **(b)** $\boldsymbol{p} = (x_\mathrm{M}, y_\mathrm{M}, d) = \left(\frac{L}{2}, y_\mathrm{M}, \frac{W}{4}\right)$

Figure 6: Stress concentration factor K_tg for a circular hole depending on its parameters $\boldsymbol{p}$

with $1 \leq w/l \leq 8$ and

$$\begin{aligned} C_1 &= 1.109 - 0.188\sqrt{w/l} + 2.086 w/l \\ C_2 &= -0.486 + 0.213\sqrt{w/l} - 2.588 w/l \\ C_3 &= 3.816 - 5.510\sqrt{w/l} + 4.638 w/l \\ C_4 &= -2.438 + 5.485\sqrt{w/l} - 4.126 w/l \\ f_\mathrm{nom} &= \frac{\sqrt{1-(w/(2y_\mathrm{M}))^2}}{1-w/(2y_\mathrm{M})} \frac{1-y_\mathrm{M}/W}{1-y_\mathrm{M}/W\left[2-\sqrt{1-(w/(2y_\mathrm{M}))^2}\right]} \end{aligned}$$

In Fig. 7a and Fig. 7b, the hole width $w \in (0, W)$ and the hole length $l \in (0, 0.6L]$ vary while the hole is located centrally in the plate with $x_\mathrm{M} = L/2$, $y_\mathrm{M} = W/2$ and $\phi = 0$. In both cases, the shading represents the parameter which is not shown on the x-axis. The reference solution [12] is only given for a fractional amount of parameter combinations which are enveloped by the results in this study. K_tg increases with increasing hole width w and with decreasing hole length l. That means that the stress concentration can also be less than for a circular hole if the elliptical hole is stretched in x-direction. The limit values are given as:

$$\lim_{w\to 0} K_\mathrm{tg} = \begin{cases} 3 \ (l = w) \\ 1 \ (l > w) \end{cases}, \quad \lim_{l\to 0} K_\mathrm{tg} \to \infty \ (w > l), \quad \lim_{w\to W} K_\mathrm{tg} \to \infty \tag{9}$$

K_tg is evaluated for varying locations $y_\mathrm{M} \in (W/8, W/2]$ with $l = W/8$, $w = W/4$ and $\phi = 0$ whereby K_tg is always higher than for a circular hole and increases with increasing eccentricity, see Fig. 7c. Except for very high eccentricities for which K_tg goes theoretically to infinity, the numerical model is in good agreement with the reference solution [12].

The dependance of K_tg on the rotation angle $\phi \in [0°, 90°]$ for a centric hole with $l = W/8$ and $w = W/4$ is displayed in Fig. 7d. Since [12] does not consider a rotation, only the value for $\phi = 0$ is given. Obviously the rotation from a vertically oriented elliptical hole to a horizontally oriented one decreases the stress concentration to a value less than for a circular hole of same width.

3.2.4 Slotted hole

The slotted hole is a combination of a rectangle and semicircles at its end. Just like an elliptical hole, the parameterization is given by the centroid coordinates $(x_\mathrm{M}, y_\mathrm{M})$, the length l, the width w and the rotation angle ϕ in the x-y-plane, see Fig. 5e. The varying parameters in the displayed tests in Fig. 8 are equal to those for Fig. 7 in section 3.2.3. As a difference, reference solutions for

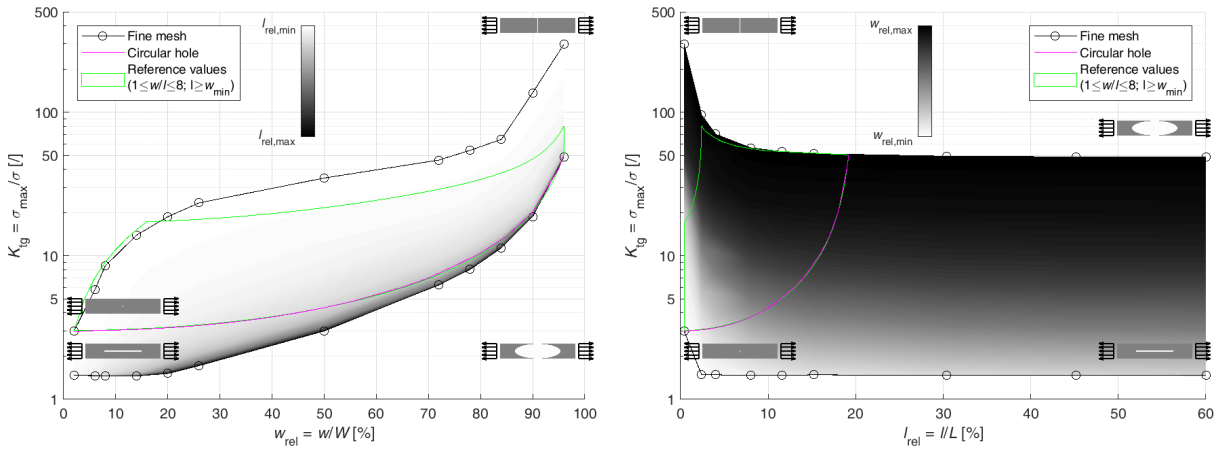

(a) $\boldsymbol{p} = (x_\mathrm{M}, y_\mathrm{M}, l, w, \phi) = \left(\frac{L}{2}, \frac{W}{2}, l, w, 0\right)$

(b) $\boldsymbol{p} = (x_\mathrm{M}, y_\mathrm{M}, l, w, \phi) = \left(\frac{L}{2}, \frac{W}{2}, l, w, 0\right)$

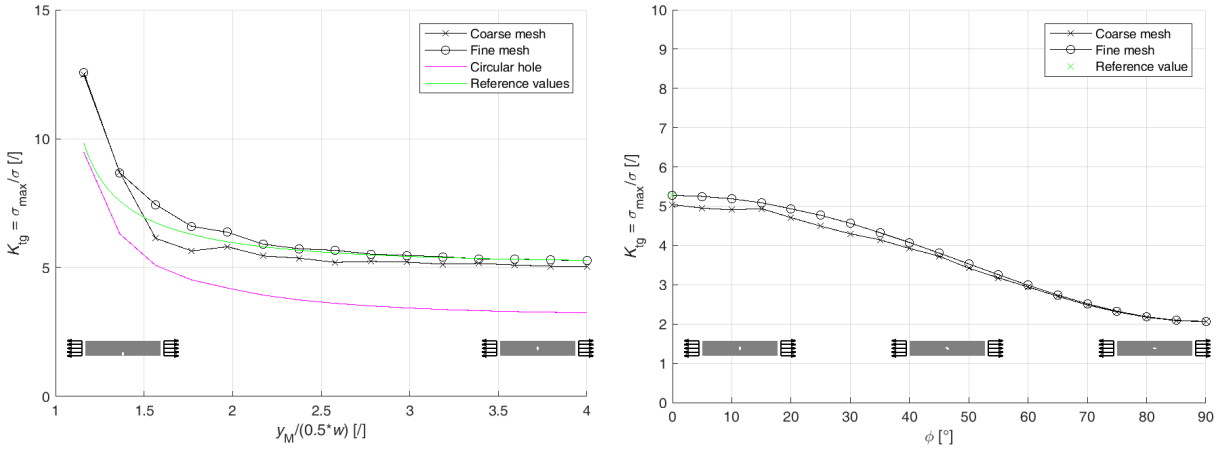

(c) $\boldsymbol{p} = (x_\mathrm{M}, y_\mathrm{M}, l, w, \phi) = \left(\frac{L}{2}, y_\mathrm{M}, \frac{W}{8}, \frac{W}{4}, 0\right)$

(d) $\boldsymbol{p} = (x_\mathrm{M}, y_\mathrm{M}, l, w, \phi) = \left(\frac{L}{2}, \frac{W}{2}, \frac{W}{8}, \frac{W}{4}, \phi\right)$

Figure 7: Stress concentration factor K_tg for an elliptical hole depending on its parameters $\boldsymbol{p}$

a slotted hole are only given for a plate with infinite width [23] based on the "equivalent ellipse" concept [23, 3], so they do not include the influence of the plate width W:

$$K_{\mathrm{tg}} = C_1 + C_2 \left(\frac{l}{w}\right) + C_3 \left(\frac{l}{w}\right)^2 + C_4 \left(\frac{l}{w}\right)^3 \tag{10}$$

with $1 \leq w/l \leq 5$ and

$$\begin{aligned} C_1 &= 14.815 - 22.308\sqrt{r/l} + 16.298 r/l \\ C_2 &= -11.201 - 13.789\sqrt{r/l} + 19.200 r/l \\ C_3 &= 0.202 + 54.620\sqrt{r/l} - 54.748 r/l \\ C_4 &= 3.232 - 32.530\sqrt{r/l} + 30.964 r/l \\ r &= l/2 \end{aligned}$$

In spite of similar trends to equal limit values (see Eq. (9)) there are some differences to mention while comparing $K_{\mathrm{tg,SH}}$ due to a slotted hole (SH) with $K_{\mathrm{tg,EH}}$ due to an elliptical hole (EH):

- for a vertically oriented hole ($w > l, \phi = 0$): $K_{\mathrm{tg,SH}} < K_{\mathrm{tg,EH}}$
- for a horizontally oriented hole ($w < l, \phi = 0$)
  - for $w < W/2$: $K_{\mathrm{tg,SH}} > K_{\mathrm{tg,EH}}$
  - for $w > W/2$: $K_{\mathrm{tg,SH}} < K_{\mathrm{tg,EH}}$

Same results can be seen while varying the rotation angle ϕ in Fig. 7d and Fig. 8d. The hole is vertically oriented for $\phi < 45°$, so $K_{\mathrm{tg,SH}} < K_{\mathrm{tg,EH}}$ and horizontally oriented for $\phi > 45°$, hence $K_{\mathrm{tg,SH}} > K_{\mathrm{tg,EH}}$.

3.2.5 Rounded rectangular hole

As an extension to a slotted hole, a hole can be described as a rounded rectangular hole by introducing a corner radius r, see Fig. 5f. The radius can take values between $r = 0$ (rectangle) and $r = \min(w/2, l/2)$ (slotted hole). In Fig. 9, the reference values are calculated based on Eq. (10) [23]. The shading represents the range of possible corner radii r whereby obviously $r = 0$ leads to $K_{\mathrm{tg}} \to \infty$. In Fig. 9a, the stress concentration factor K_{tg} is evaluated for an eccentric rounded rectangular hole with constant values $w = W/4$, $l = W/8$, $\phi = 0$ and varying values y_{M} and r. Fig. 9b shows K_{tg} depending on ϕ and r with constant values $x_{\mathrm{M}} = L/2$, $y_{\mathrm{M}} = W/2$, $w = W/4$ and $l = W/8$. In all cases, the lowest values for K_{tg} can be found near the solution for a slotted hole, consequently a smaller corner radius and sharper edges result in a higher stress concentration factor.

4 Comparison of stress concentrations based on different hole shape parameterizations

4.1 Arbitrary hole shapes and shape fitting algorithm

Referring to section 2, holes with arbitrary shapes can be detected by means of non-destructive testing like ultrasonic or computer tomographic scanning. In spite of high scan resolutions, only a finite number of points $\boldsymbol{x} = (x_i, y_i)$ $(i = 1 \cdots n)$ can be acquired in a quasi-continuous measurement. In this study, two exemplary holes with 15 and 11 points, respectively, are considered in a plate with a width of $W = 50$mm and a length of $L = 5W = 250$mm, see Fig. 10. The points are connected by splines [7]. In addition to determine the convex hull, different hole shapes as

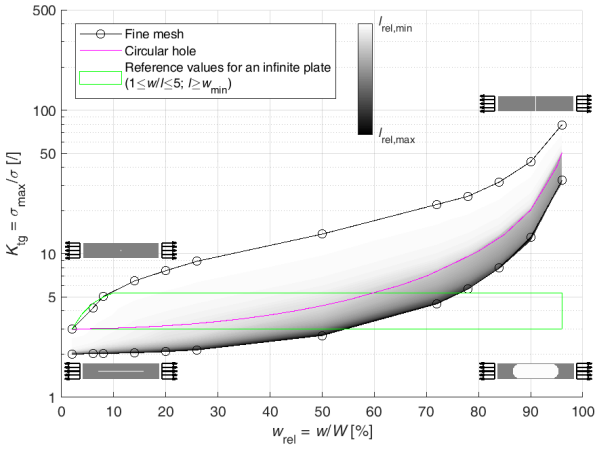

(a) $\boldsymbol{p} = (x_\mathrm{M}, y_\mathrm{M}, l, w, \phi) = \left(\frac{L}{2}, \frac{W}{2}, l, w, 0\right)$

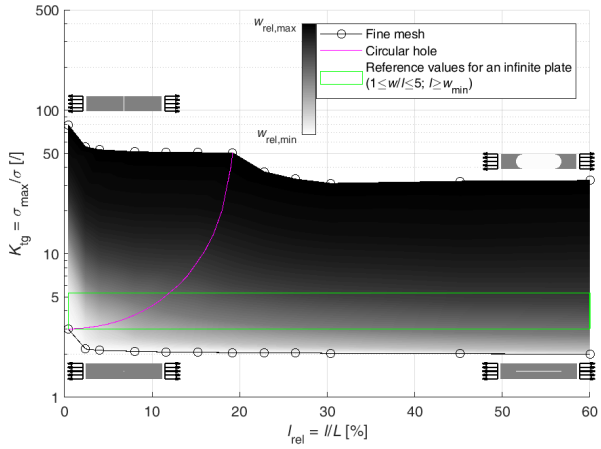

(b) $\boldsymbol{p} = (x_\mathrm{M}, y_\mathrm{M}, l, w, \phi) = \left(\frac{L}{2}, \frac{W}{2}, l, w, 0\right)$

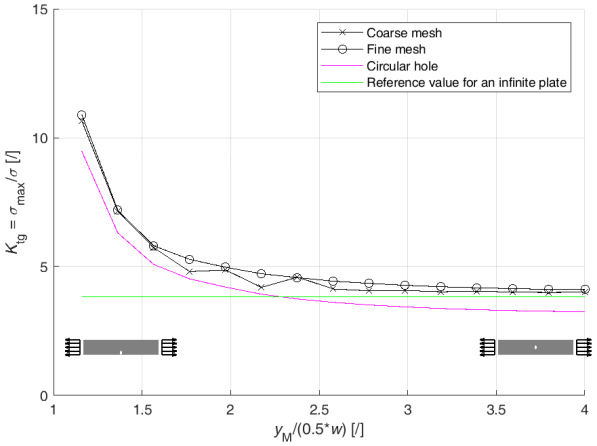

(c) $\boldsymbol{p} = (x_\mathrm{M}, y_\mathrm{M}, l, w, \phi) = \left(\frac{L}{2}, y_\mathrm{M}, \frac{W}{8}, \frac{W}{4}, 0\right)$

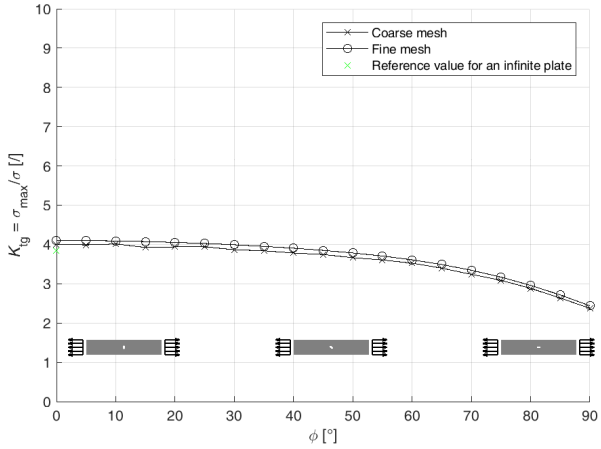

(d) $\boldsymbol{p} = (x_\mathrm{M}, y_\mathrm{M}, l, w, \phi) = \left(\frac{L}{2}, \frac{W}{2}, \frac{W}{8}, \frac{W}{4}, \phi\right)$

Figure 8: Stress concentration factor K_tg for a slotted hole depending on its parameters $\boldsymbol{p}$

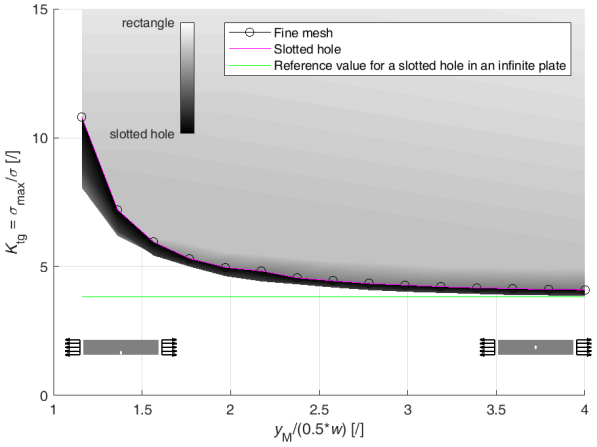

(a) $\boldsymbol{p} = (x_\mathrm{M}, y_\mathrm{M}, l, w, \phi, r) = \left(\frac{L}{2}, y_\mathrm{M}, \frac{W}{8}, \frac{W}{4}, 0, r\right)$

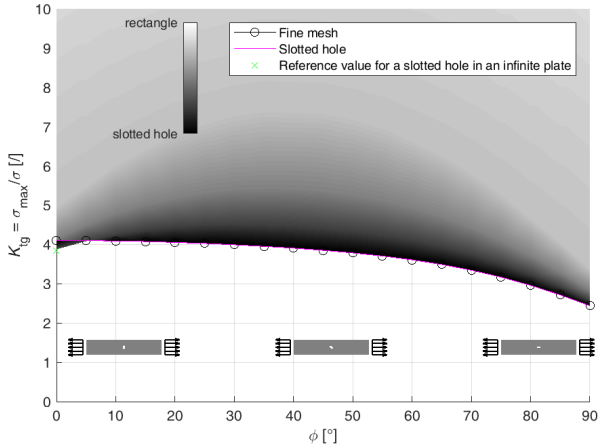

(b) $\boldsymbol{p} = (x_\mathrm{M}, y_\mathrm{M}, l, w, \phi, r) = \left(\frac{L}{2}, \frac{W}{2}, \frac{W}{8}, \frac{W}{4}, \phi, r\right)$

Figure 9: Stress concentration factor K_tg for a rounded rectangular hole depending on its parameters $\boldsymbol{p}$

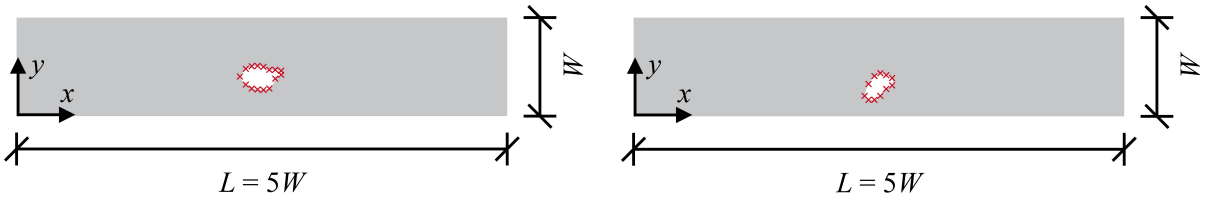

(a) Hole 1 **(b)** Hole 2

Figure 10: Exemplary holes with arbitrary shapes

described in section 3.2 can be fitted to the given points $\boldsymbol{x}$ using a least-square optimization algorithm. For each shape $s = \{\text{circular hole, elliptical hole, slotted hole, rounded rectangular hole}\}$, the following global optimization problem is solved to determine the optimal shape parameters $\boldsymbol{p}_{\text{opt}}$:

$$z_{\text{opt}}(s) = z(\boldsymbol{p}_{\text{opt}}) = \min_{\boldsymbol{p} \in R} \left(z = \sum_{i=1}^{n} \min \left(\|\boldsymbol{t} - (x_i, y_i)\|_2^2 \right) \mid \boldsymbol{p} \in R \right) \tag{11}$$

with

		$\|\cdot\|_2$	euclidean L2-norm
$\boldsymbol{p}$	=	$\boldsymbol{p}(s)$	hole parameters, see section 3.2
$\boldsymbol{t}$	=	$\boldsymbol{t}(s, \boldsymbol{p})$	points on hole boundary ∂H
R	=	$R(s)$	design space: $x_{\text{M}} \in (W, L - W)$, $y_{\text{M}} \in (0, W)$, $d > 0$, $l > 0$, $w > 0$, $\phi \in [0°, 360°]$, $r \geq 0$

4.2 Shape parameterizations and resulting stress concentrations

As an advantage, the shape fitting leads to a small number of needed parameters for describing the hole H with boundary ∂H. Furthermore, the meshing is in general less error-prone than for an arbitrary one within a structural finite element analysis. However, some differences concerning the stress concentration factor K_{tg} and the location $c(\boldsymbol{x}_{\max})$ of the maximum stress in the structure exist. In Table 1 for hole 1 or respectively in Table 2 for hole 2, the different shapes s with their optimal parameters $\boldsymbol{p}_{\text{opt}}$, the corresponding objective function value z_{opt}, the stress concentration factor K_{tg} with the deviation to the original arbitrary shape in brackets and the location of the maximum first principal stress $c(\boldsymbol{x}_{\max})$ are shown. The underlying models are displayed in Fig. 11 and Fig. 12.

Comparing the shape parameterizations based on the objective function value z_{opt}, it is obvious that the rounded rectangular hole is always better than the slotted hole due to the corner radius r as additional design parameter. Analogously, the slotted hole as well as the elliptical hole fit an arbitrary hole always better than a circular one. Regarding the rounded rectangular, slotted and elliptical hole, it is to mention that a switch of l and w and a change of $\phi \pm 90°$ at once or a single change of $\phi \pm 180°$ lead to the same shape. Concerning the stress concentration, the impact of the shape and their parameters has been shown in detail in section 3.2. However, a direct correlation between z_{opt} and K_{tg} is not identifiable. It can generally be noted that the original arbitrary shape has to be sufficiently smooth to ensure satisfactory results with simplified hole shapes. Sharp-edged or jagged shapes would be smoothed with a significantly lower stress concentration.

For both holes, the location parameters x_{M} and y_{M} show almost identical results regardless of the underlying shape s. Concerning z_{opt}, the rounded rectangular hole is the best while the circular hole is the worst shape fit, but since the corner radius take on a small value ($r = 0$mm for hole 1, $r = 1.6$mm for hole 2), K_{tg} deviates significantly from the original value. From that standpoint, the circular hole shape for hole 1 or respectively the slotted hole shape for hole 2 have the smallest deviations. The location of the maximum stress expressed by $c(\boldsymbol{x}_{\max})$ is correctly identified for hole 1. For hole 2, the maximum stresses above (4.44875) and below (4.39892)

the arbitrary shape are very similar which causes the switch to the opposite side with less edge distance for the simplified hole shapes.

Table 1: Different optimal hole shapes and their stress concentration for hole 1

Shape s	Optimal shape parameters $\boldsymbol{p}_{\text{opt}}$ ([mm] / [°])	z_{opt} [/]
arbitrary	-	-
convex	-	-
circular	$(x_{\text{M}}, y_{\text{M}}, r) = (124.4, 19.6, 7.8)$	43.307
elliptical	$(x_{\text{M}}, y_{\text{M}}, l, w, \phi) = (124.0, 19.6, 20.5, 11.7, 3.2)$	11.177
slotted	$(x_{\text{M}}, y_{\text{M}}, l, w, \phi) = (124.2, 19.5, 11.1, 19.7, 86.2)$	12.533
rounded rectangular	$(x_{\text{M}}, y_{\text{M}}, l, w, \phi, r) = (124.1, 19.4, 18.3, 10.9, 167.9, 0.0)$	9.334
Shape s	**K_{tg} [/]**	**$c(\mathbf{x}_{\max})$**
arbitrary	3.57055	below
convex	3.23584 (-9.37%)	below
circular	3.67447 $(+2.91\%)$	below
elliptical	2.52351 (-29.32%)	below
slotted	2.94374 (-17.55%)	below
rounded rectangular	$\to \infty$	below & above

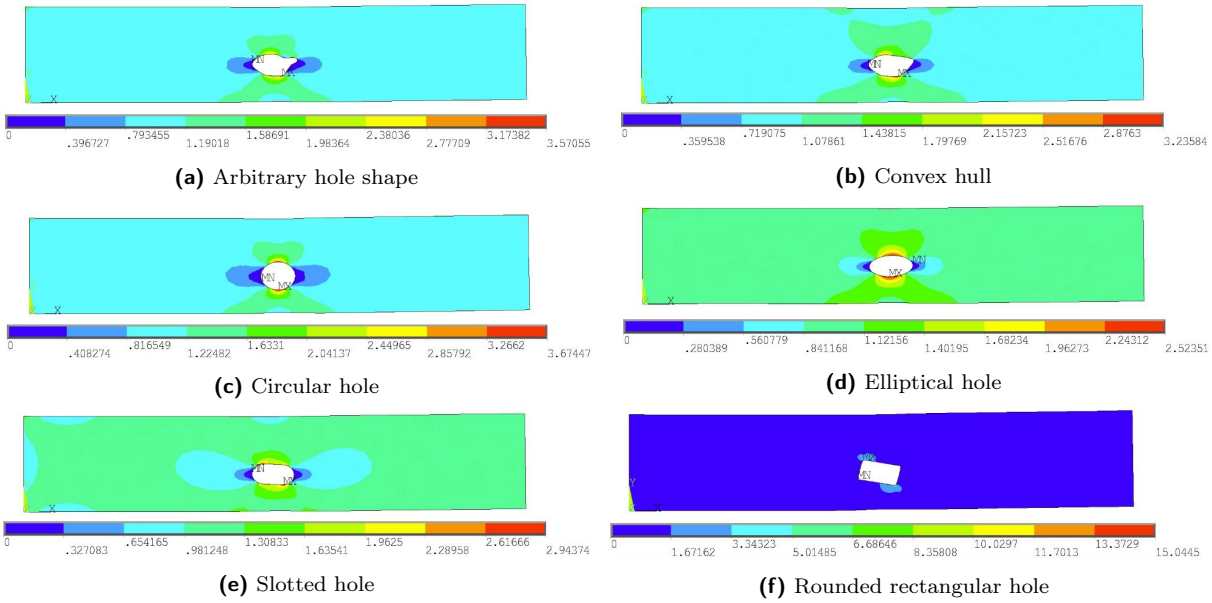

(a) Arbitrary hole shape

(b) Convex hull

(c) Circular hole

(d) Elliptical hole

(e) Slotted hole

(f) Rounded rectangular hole

Figure 11: First principal stress field and its maximum for hole 1

5 Analysis of the stress concentration under polymorphic uncertainties

5.1 Aleatory and epistemic uncertainties

The detection of air voids within a structure as well as the quantification of their properties by using non-destructive testing are influenced by diverse uncertainties [6]. Therefore, a numerical uncertainty model is proposed to evaluate the stress concentration with regard to present air voids.

In the following, the number of air voids is reduced to $n = 1$ like in section 3 and 4 and the hole shapes $s = \{$circular hole, elliptical hole, slotted hole$\}$ are considered. Although the rounded rectangular hole has fitted the arbitrary holes 1 and 2 at its best, it has shown significantly higher

Table 2: Different optimal hole shapes and their stress concentration for hole 2

Shape s	Optimal shape parameters $\boldsymbol{p}_{\text{opt}}$ ([mm] / [°])	z_{opt} [/]
arbitrary	-	-
convex	-	-
circular	$(x_{\text{M}}, y_{\text{M}}, r) = (124.4, 15.7, 6.6)$	21.188
elliptical	$(x_{\text{M}}, y_{\text{M}}, l, w, \phi) = (124.5, 15.7, 9.6, 17.0, 131.6)$	3.015
slotted	$(x_{\text{M}}, y_{\text{M}}, l, w, \phi) = (124.4, 16.0, 16.4, 8.8, 42.5)$	2.032
rounded rectangular	$(x_{\text{M}}, y_{\text{M}}, l, w, \phi, r) = (124.2, 15.7, 15.8, 8.5, 42.5, 1.6)$	1.700
Shape s	**K_{tg} [/]**	**$c(\mathbf{x}_{\max})$**
arbitrary	4.44875	above
convex	4.51347 $(+1,45\%)$	below
circular	3.75610 (-15.57%)	below
elliptical	4.04076 (-9.17%)	below
slotted	4.48725 $(+0.87\%)$	below
rounded rectangular	7.23700 $(+62.67\%)$	below

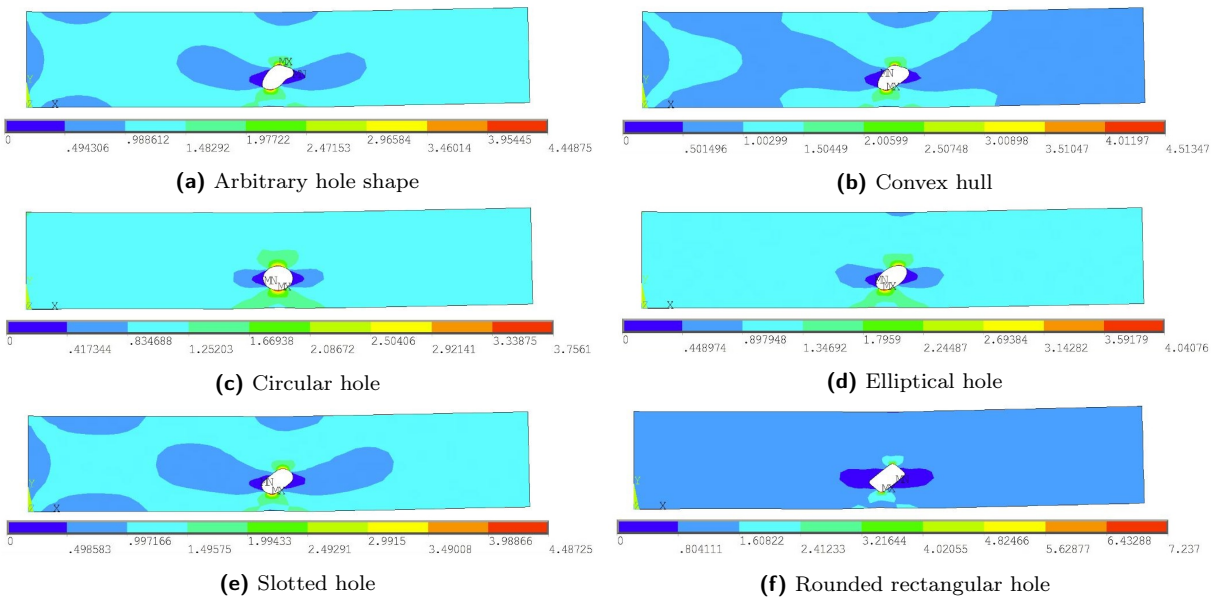

(a) Arbitrary hole shape

(b) Convex hull

(c) Circular hole

(d) Elliptical hole

(e) Slotted hole

(f) Rounded rectangular hole

Figure 12: First principal stress field and its maximum for hole 2

stress concentrations due to sharped edges in the deterministic cases in section 4. The uncertain shape parameters $\boldsymbol{p}(s)$ are divided into location parameters $(x_\mathrm{M}, y_\mathrm{M})$, orientation parameter ϕ and size parameters (r, l, w). Even if the location and orientation could also be detected by CT scanning, they are subject to randomness and natural variability, thus leading to aleatory uncertainties described by stochastic variables. By contrast, the size parameters can be seen as epistemic uncertainties resulting from a certain manufacturing process, which are measurable on a limited amount of air voids. Due to the given resolution of $\Delta = 3\mathrm{mm}$ in the conducted CT scanning, interval variables are defined for the size parameters of the best-fit shapes. The actual size parameters are larger than the measurable ones which leads to:

$$\begin{aligned} r_i &= [r_{i,\mathrm{Fit}}, r_{i,\mathrm{Fit}} + \Delta]\,, \\ l_i &= [l_{i,\mathrm{Fit}}, l_{i,\mathrm{Fit}} + 2\Delta]\,, \\ w_i &= [w_{i,\mathrm{Fit}}, w_{i,\mathrm{Fit}} + 2\Delta]\,. \end{aligned} \tag{12}$$

In Table 3, all uncertain parameters for the arbitrary holes 1 and 2 of section 4 are displayed. It should be mentioned that Eq. (1) has to be fulfilled.

Table 3: Different hole shapes and their uncertain parameters for hole 1 and hole 2

Shape s	aleatory uncertainties stochastic variables ([mm] / [°])	epistemic uncertainties interval variables [mm]	
circular	$x_\mathrm{M} \sim \mathcal{U}(50, 200)$ $y_\mathrm{M} \sim \mathcal{U}(0, 50)$	$r_1 = [7.8, 10.8]$	$r_2 = [6.6, 9.6]$
elliptical	$x_\mathrm{M} \sim \mathcal{U}(50, 200)$ $y_\mathrm{M} \sim \mathcal{U}(0, 50)$ $\phi \sim \mathcal{U}(0, 360)$	$l_1 = [20.5, 26.5]$ $w_1 = [11.7, 17.7]$	$l_2 = [9.6, 15.6]$ $w_2 = [17.0, 23.0]$
slotted	$x_\mathrm{M} \sim \mathcal{U}(50, 200)$ $y_\mathrm{M} \sim \mathcal{U}(0, 50)$ $\phi \sim \mathcal{U}(0, 360)$	$l_1 = [11.1, 17.1]$ $w_1 = [19.7, 25.7]$	$l_2 = [16.4, 22.4]$ $w_2 = [8.8, 14.8]$

5.2 Results

Obviously, the location of the maximum first principal stress expressed by $c(\mathbf{x}_\mathrm{max}) = \{\mathrm{above}, \mathrm{below}\}$ mainly depends on the uncertain input y_M. Since y_M is uniformly distributed, an equal frequency of *above* and *below* is expected. Therefore, the focus is on the analysis of the stress concentration factor K_tg. The presented problem under polymorphic uncertainties require a stochastic analysis on each point in interval space for each underlying shape s. Monotony of K_tg with regard to the size parameters is presumed which enables the vertex method [4] for the analysis in the interval space. For the stochastic parameters, a classical Monte-Carlo sampling approach [8] with $n_\mathrm{MC} = 10^3$ samples on each point in interval space is implemented. To reduce the computational costs in consideration of the accuracy, a surrogate model $K_\mathrm{tg} \rightarrow \widetilde{K}_\mathrm{tg}$ is additionally used based on section 3. For given size parameters, a tensor product grid of ten equally distributed points for each stochastic variable is constructed considering the symmetrical behavior of K_tg with regard to y_M and ϕ. The variable x_M is not taken into account [24]. On this basis, a cubic spline interpolation is used as approximation function [17] which is finally evaluated $n_\mathrm{Surr} = 10^6$ times on each point in interval space. Other surrogate models, e.g. based on artificial neural networks (ANN) within a response surface method [5] could potentially increase the efficiency. This extension is going beyond the scope of the present study.

For both holes, the slotted hole evaluation is exemplarily displayed in Fig. 13, as well as the interval-stochastic stress concentration factor K_tg. The surrogate model requires much less finite element simulations than the classical sampling approach but leads to a similar result. The differences are negligible. Comparing the bounds of the interval mean in the second and forth row

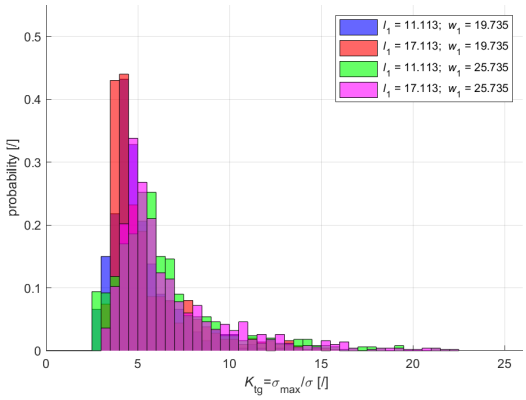

(a) Hole 1: Monte-Carlo & slotted hole

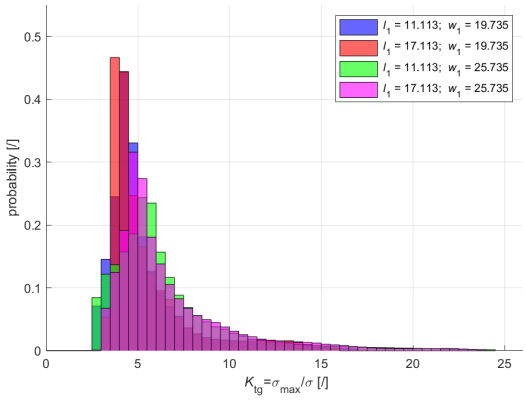

(b) Hole 1: Surrogate & slotted hole

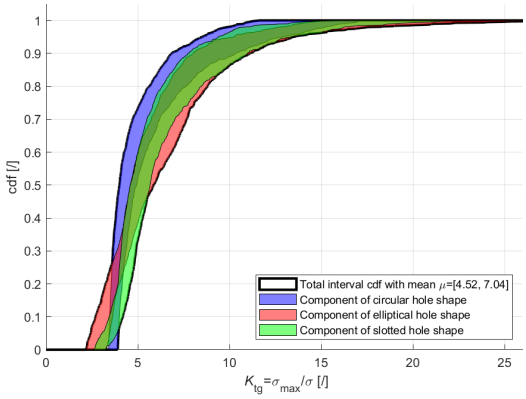

(c) Hole 1: Monte-Carlo & interval cdf

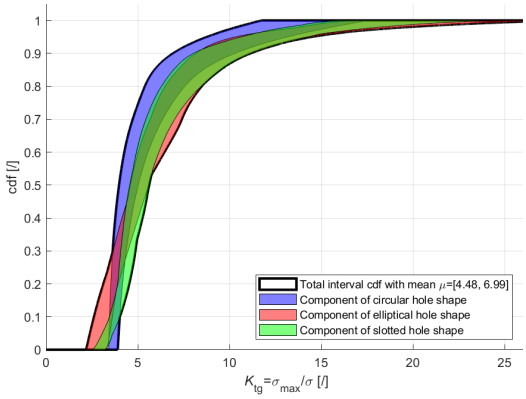

(d) Hole 1: Surrogate & interval cdf

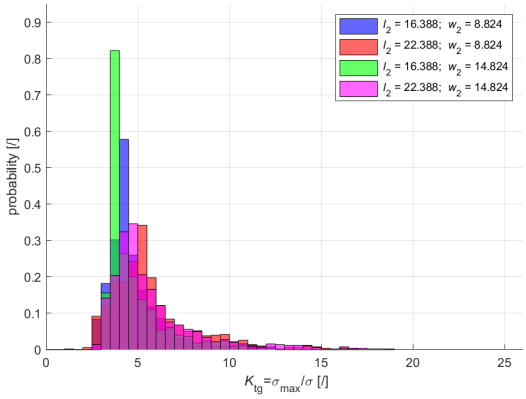

(e) Hole 2: Monte-Carlo & slotted hole

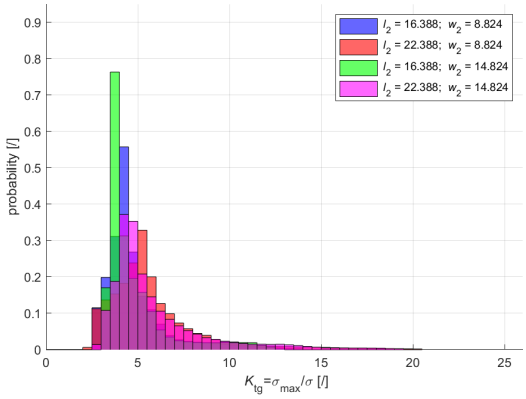

(f) Hole 2: Surrogate & slotted hole

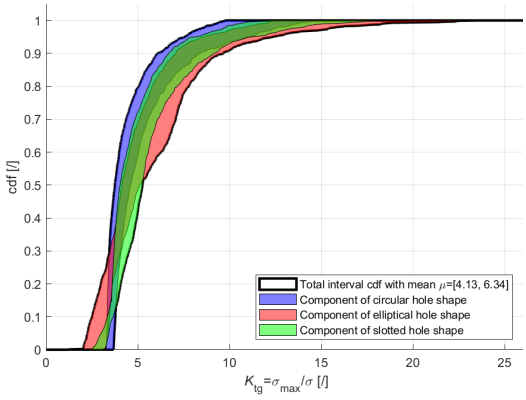

(g) Hole 2: Monte-Carlo & interval cdf

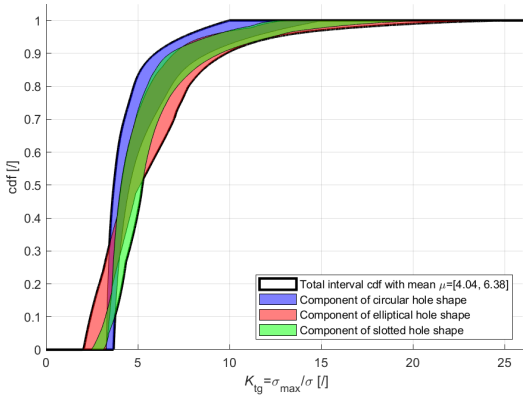

(h) Hole 2: Surrogate & interval cdf

Figure 13: Slotted hole evaluation and interval-stochastic K_{tg} (first two rows: hole 1, last two rows: hole 2, left column: sampling approach, right column: surrogate modeling)

in Fig. 13, a maximum variance of 2% is recognizable which validates the used surrogate model. Due to smaller size parameters for hole 2 compared to hole 1, the stress concentration factor is even smaller, visible in approximately 10% smaller bounds for the mean. Furthermore, the interval cdf's show similar trends. The total interval cdf is the envelope of all considered shapes, whereby no individual result is completely enveloped by another one. On the upper bound of K_{tg}, defined as worst-case, all hole shapes are represented which justifies the hole shape to be an essential uncertain parameter.

6 Conclusions

Air void inclusions with arbitrary shapes are present in many different materials, e.g. in adhesive bonds of rotor blades resulting from a certain manufacturing process. In engineering applications, they can influence significantly the structural integrity and at worst, lead to structural failure caused by stress concentrations around them. A linear elastostatic boundary value problem for a perforated 2D plate is defined to investigate the impact of different hole shapes on the stress concentration factor and on the location of the maximum first principal stress. By using a least-square optimization algorithm, circular, elliptical, slotted and rounded rectangular holes are fitted on two sufficiently smooth arbitrary holes which have been detected by CT scanning of adhesive bonds. It could be seen that the rounded rectangular hole overestimates the stress concentration due to a small best-fit corner radius. Furthermore, the location of the maximum first principal stress can change to the side with less edge distance while shape fitting. The extension to a problem under polymorphic uncertainties by classifying the shape parameters into aleatory and epistemic uncertainties has shown the importance of the consideration of different hole shapes. A defined surrogate model based on cubic spline interpolation has improved the efficiency without loss of accuracy.

7 Future work

The authors are currently working on the efficient generation of arbitrary shapes and on the extension of perforated structures to multi-scale models. Also the development of further surrogate models for solving problems under polymorphic uncertainties is an ongoing work and will be presented in future.

Acknowledgement

The authors gratefully acknowledge the financial support of the German Research Foundation (DFG) within the Priority Programme "Polymorphic uncertainty modelling for the numerical design of structures – SPP 1886".

The contribution was enriched by helpful discussions with our colleagues Dietmar Hömberg, Martin Eigel and Robert Gruhlke from *Weierstraß-Institut für Angewandte Analysis und Stochastik (WIAS) Berlin* within our collaborative project "MuScaBlaDes: Multi-scale failure analysis with polymorphic uncertainties for optimal design of rotor blades".

References

[1] K. C. Bacharoudis and T. P. Philippidis. A probabilistic approach for strength and stability evaluation of wind turbine rotor blades in ultimate loading. *Structural Safety*, 40:31–38, 2013.

[2] M. Beer, S. Ferson, and V. Kreinovich. Imprecise probabilities in engineering analyses. *Mechanical Systems and Signal Processing*, 37:4–29, 2013.

[3] H. L. Cox. *Four Studies in the Theory of Stress Concentration.* H.M. Stationery Office, 1953.

[4] W. Dong and H. C. Shah. Vertex method for computing functions of variables. *Elsevier Science Publishers*, 24:65–78, 1987.

[5] M. Drieschner, R. Gruhlke, Y. Petryna, M. Eigel, and D. Hömberg. Comparison of various monomorphic and polymorphic approaches for uncertainty quantification with experimental investigations. *WIAS Preprint*, 2019.

[6] M. Drieschner and Y. Petryna. Acquisition of polymorphic uncertain data based on computer tomographic scans and integration in numerical models of adhesive bonds. *Preprint-Reihe des Fachgebiets Statik und Dynamik, Technische Universität Berlin*, Preprint No. 2019-01, 2019. http://dx.doi.org/10.14279/depositonce-8235.

[7] N. Ezhov, F. Neitzel, and S. Petrovic. Spline Approximation, Part 1: Basic Methodology. *Journal of Applied Geodesy*, 12:139–155, 2018.

[8] J. E. Gentle. *Random Number Generation and Monte Carlo Methods.* Springer, 2 edition, 2003.

[9] W. Graf, M. Götz, and M. Kaliske. Analysis of dynamical processes under consideration of polymorphic uncertainty. *Structural Safety*, 52:194–201, 2015.

[10] R. C. J. Howland and L. N. G. Filon. On the stresses in the neighborhood of a circular hole in a strip under tension. *Philosophical Transactions of the Royal Society of London, Series A*, 229:49–86, 1930.

[11] IEC: International Electrotechnical Commission. Wind turbines - Part 23: Full-scale structural testing of rotor blades (IEC 61400-23:2014), April 2014.

[12] M. Isida. Form factors of a strip with an elliptic hole in tension and bending. *Sci. Pap. Faculty Engr. Tokushima Univ.*, 4:70, 1953.

[13] E. Kirsch. Die Theorie der Elastizität und die Bedürfnisse der Festigkeitslehre. *Zeitschrift des Vereines deutscher Ingenieure*, 42:797–807, 1898.

[14] D. Kovačević, Y. Petryna, and M. Petronijević. Assessment of the impact of air voids on adhesive joints in rotor blades by use of NDT and FEA. *EWSHM 2016*, 2016.

[15] A. Künzel. *Parameteridentifikation auf Basis faseroptisch gemessener quasi-kontinuierlicher Dehnungssignale.* PhD thesis, Techische Universität Berlin, 2016.

[16] O. P. LeMaître and O. M. Knio. *Spectral Methods for Uncertainty Quantification.* Springer, 2010.

[17] MATLAB®. *Curve Fitting Toolbox™.* The MathWorks® Inc., 2017.

[18] B. Möller and M. Beer. *Fuzzy Randomness - Uncertainty in Civil Engineering and Computational Mechanics.* Springer, 2004.

[19] Y. Petryna. Automatisiertes Verfahren für serienmäßige Integritätsprüfung von Rotorblättern und Bereitstellung von Rotorblatt-Tunern - Abschlussbericht. Technical report, TU Berlin, BAM - Bundesanstalt für Materialforschung und -prüfung and Steinbichler Optotechnik GmbH, 2015.

[20] W. D. Pilkey and D. F. Pilkey. *Peterson's Stress Concentration Factors, Third Edition.* John Wiley & Sons, Inc., 2008.

[21] F. Sayer, A. Antoniou, and A. van Wingerde. Investigation of structural bond lines in wind turbine blades by sub-component tests. *Adhesion and Adhesives*, 37:129–135, 2012.

[22] S. Sjöström. *On the stresses at the edge of an eccentrically located circular hole in a strip under tension*. Flygtekn, 1950.

[23] A. Sobey. Stress concentration factors for rounded rectangular holes in infinite sheets. *Her Majesty's Stationary Office*, page 3407, 1963.

[24] N. Troyani, C. Gomes, and G. Sterlacci. Theoretical stress concentration factors for short rectangular plates with centered circular holes. *Journal of Mechanical Design*, 124(1):126–128, 1999.

[25] C. Wang and Z. Qiu. Hybrid uncertain analysis for temperature field prediction with random, fuzzy and interval parameters. *International Journal of Thermal Sciences*, 98:124–134, 2015.

[26] C. Wang, Z. Qiu, and Y. He. Fuzzy stochastic finite element method for the hybrid uncertain temperature field prediction. *International Journal of Heat and Mass Transfer*, 91:512–519, 2015.

[27] D. Xiu. *Numerical Methods for Stochastic Computation*. Princeton University Press, 2010.

[28] J. Yang, C. Peng, J. Xiao, J. Zeng, S. Xing, J. Jin, and H. Deng. Structural investigation of composite wind turbine blade considering structural collapse in full-scale static tests. *Composite Structures*, 97:15–29, 2013.

[29] D. S. Zarouchas, A. A. Makris, F. Sayer, D. V. Hemelrijck, and A. van Wingerde. Investigations on the mechanical behavior of a wind rotor blade subcomponent. *Composites: Part B*, 43:647–654, 2012.